Peak-locking error reduction by birefringent optical diffusers

Kislaya, Ankur; Sciacchitano, Andrea

DOI
10.1088/1361-6501/aa97f7

Publication date
2018

Document Version
Final published version

Published in
Measurement Science and Technology

Measurement Science and Technology

PAPER

Peak-locking error reduction by birefringent optical diffusers

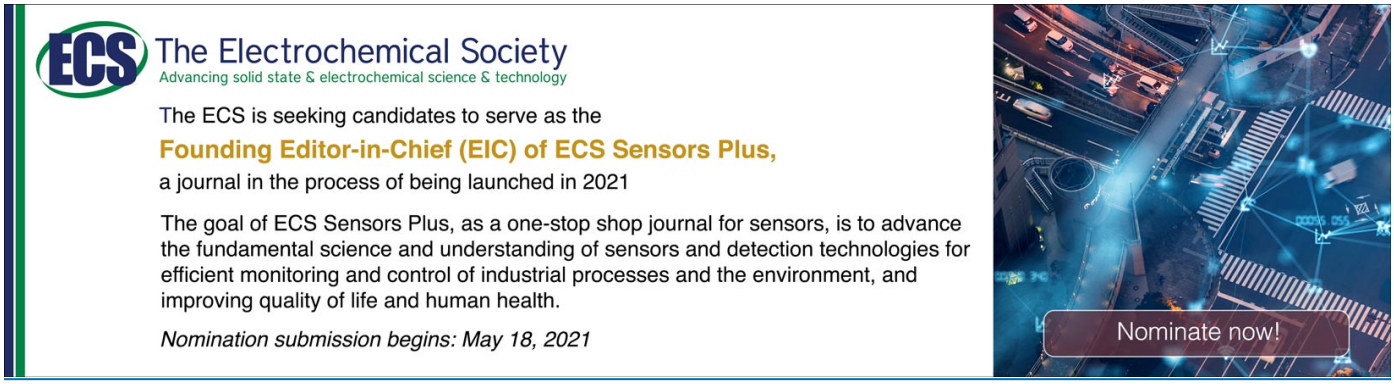

IOP Publishing Measurement Science and Technology
Meas. Sci. Technol. **29** (2018) 025202 (9pp) https://doi.org/10.1088/1361-6501/aa97f7

Peak-locking error reduction by birefringent optical diffusers

Ankur Kislaya[1] **and Andrea Sciacchitano**[2]

[1] Laboratory for Aero and Hydrodynamics, TU Delft, Delft, Netherlands
[2] Department of Aerospace Engineering, TU Delft, Delft, Netherlands

E-mail: a.kislaya@tudelft.nl

Received 24 July 2017, revised 28 October 2017
Accepted for publication 3 November 2017
Published 17 January 2018

Abstract

The use of optical diffusers for the reduction of peak-locking errors in particle image velocimetry is investigated. The working principle of the optical diffusers is based on the concept of birefringence, where the incoming rays are subject to different deflections depending on the light direction and polarization. The performances of the diffusers are assessed via wind tunnel measurements in uniform flow and wall-bounded turbulence. Comparison with best-practice image defocusing is also conducted. It is found that the optical diffusers yield an increase of the particle image diameter up to 10 μm in the sensor plane. Comparison with reference measurements showed a reduction of both random and systematic errors by a factor of 3, even at low imaging signal-to-noise ratio.

Keywords: peak locking, particle image velocimetry, optical diffusers, birefringence, random and bias errors, image defocussing

(Some figures may appear in colour only in the online journal)

1. Introduction

In digital particle image velocimetry (PIV), peak-locking is the systematic tendency of the measured particle image displacement to be biased towards the closest integer pixel value (Westerweel 1997). Such error source is mainly caused by the image digitalization process and occurs when the particle image diameter is close to the pixel size (Raffel *et al* 2007). Aside from the particle image size, peak-locking errors are caused by other parameters of the image analysis, including image interrogation algorithm (use of window shift or window deformation, Scarano and Riethmuller (1999), Gui and Wereley (2002)), image interpolation method (Roesgen 2003, Astarita and Cardone 2005, Nobach *et al* 2005), particle images truncation at the edges of the interrogation window (Nogueira *et al* 2001) and cross-correlation peak interpolation algorithm (Westerweel 1993, Christensen 2004, Fore 2010).

Although most sources of peak-locking can be dramatically reduced by using state-of-the-art interrogation algorithms with window weighting, window deformation and accurate image and correlation peak interpolation algorithms (Scarano 2002), peak-locking errors due to the small particle image diameter are still common in many PIV measurements. These errors are particularly relevant for high-speed PIV measurements conducted with CMOS cameras, where the large pixel size (11 to 20 micrometres) and small fill factor typically yield a particle image diameter not exceeding one pixel. Christensen (2004) showed that peak-locking errors strongly affect the evaluation of turbulence statistics, especially turbulent velocity fluctuations, Reynolds stresses, vortices and two-point correlation coefficients, with errors up to 0.3 pixels on the fluctuating velocities. Theoretical models for the a-priori estimation of peak-locking errors in turbulence statistics have been introduced by Angele and Muhammad-Klingmann (2005) and by Cholemari (2007), also with the attempt of reducing the systematic error.

Several approaches have been proposed to reduce peak-locking errors. Roth and Katz (2001) attempted to eliminate those by applying histogram equalization to the uneven distribution of sub-pixel displacements in a vector field. The approach has been further improved by Hearst and Ganpathisubramani (2015), who proposed to apply the histogram equalization locally along a time sequence of vector fields, instead of spatially in one vector field. However, the method is only effective for the specific cases of highly turbulent flows, where all sub-pixel displacements have the

same probability of occurrence, and in absence of other error sources. Chen and Katz (2005) introduced the correlation mapping method, where a virtual correlation function is built between first exposure and a second exposure obtained from the first image via bi-cubic interpolation. This virtual correlation is matched with the actual correlation function to obtain a peak-locking free displacement field. The approach is reported to strongly reduce peak-locking errors, although its performances strongly degrade in presence of out-of-plane motion, image noise and non-uniform particle distributions. Nogueira *et al* (2009, 2011) proposed a multiple Δt strategy, where the information obtained at different inter-frame time intervals is employed to decrease peak-locking errors. This approach suffers from two main drawbacks: (1) it requires that the acquisition is conducted at different Δt's, so it cannot be applied to data already acquired at a single inter-frame time interval; (2) it is effective only when the average flow is steady and it is focussed on providing the magnitude of the peak-locking error rather than correcting it.

In many practical situations, peak-locking errors are avoided by slightly moving the focal plane with respect to the measurement plane (i.e. defocusing the images), so to increase the particle image diameter. Overmars *et al* (2010) report that a slight image defocusing is effective in reducing the degree of peak-locking and in turn the systematic errors on the particle image displacement. However, excessive defocussing may lead to increased random errors due to the difficulty to correctly locate the particle image centroid. Furthermore, image defocusing cannot be applied in tomographic PIV, where the entire thickness of the measurement volume must be imaged in focus.

To overcome the limitations above, Michaelis *et al* (2016) introduced the use of optical diffusers to be mounted between the sensor and the lens of the camera. The diffusers have the effect of increasing the point spread function of the imaging system, thus yielding a larger particle image diameter. Results from measurements on a precision turn table showed an increase of the particle image diameter up to 50% and peak-locking error reduction by a factor of 4, similarly to best practice of image defocusing. However, the authors did not perform wind tunnel experiments on actual tracer particles. As a consequence, the question of whether optical diffusers are effective to reduce peak-locking errors for PIV measurements is still open.

The present work builds upon that of Michaelis *et al* (2016) by assessing the capability of the optical diffusers to reduce peak-locking errors in wind tunnel environment. The effect of using one or two optical diffusers is investigated via comparison with standard measurements (focused images) and with best-practice image defocusing.

2. Working principle of the optical diffusers

The optical diffusers are mounted between the lens and the sensor of the camera in order to increase the diffraction-limited particle image diameter. The working principle of the

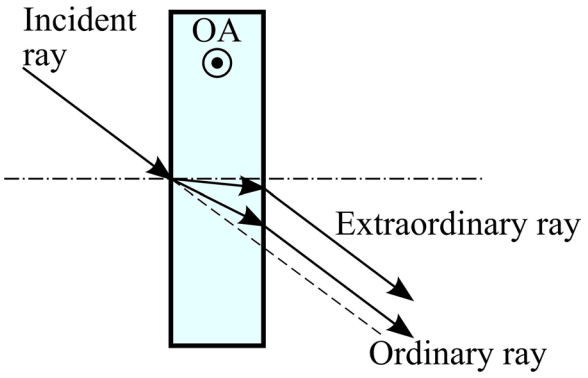

Figure 1. Ray diagram showing an incident light ray passing through a birefringent material.

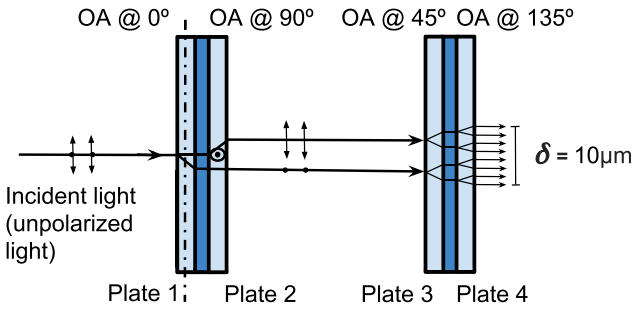

Figure 2. Schematic diagram showing an incident light ray passing through two diffusers at a relative angle of 45°.

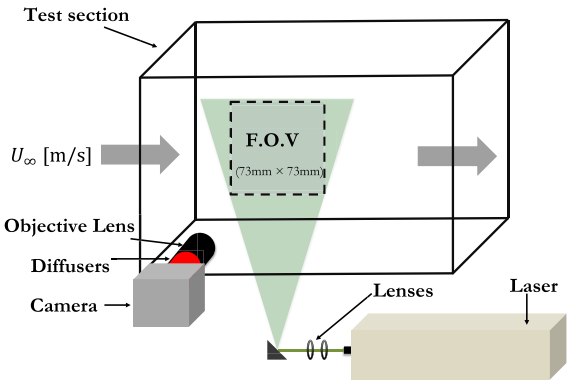

Figure 3. Schematic setup for the uniform flow test case.

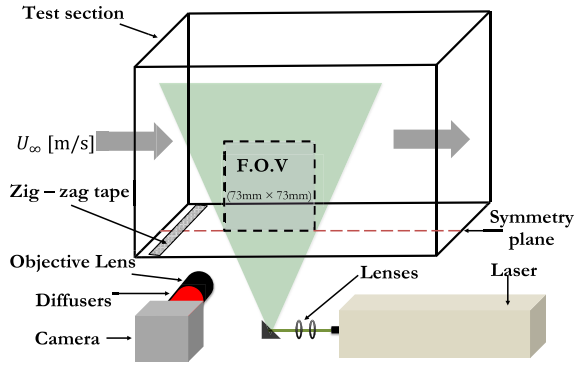

Figure 4. Schematic setup for the wall-bounded turbulence test case.

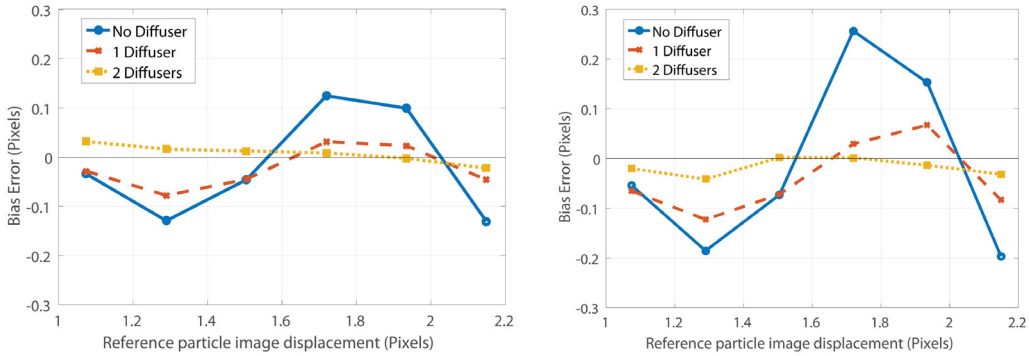

Figure 5. Bias error as a function of the particle image displacement for 0, 1 and 2 optical diffusers. Left: $f_{\#} = 4$; right: $f_{\#} = 8$.

diffuser is based on the concept of *birefringence*, which is the optical property of a material having a refractive index that depends on the polarization and propagation direction of light (Born and Wolf 1999). When the light scattered by the particles reaches the diffuser, it is split by polarization into two rays that take slightly different paths. The light whose polarization is orthogonal to the optical axis (OA) of the diffuser experiences a refractive index n_o (*ordinary ray*): its refraction is governed by Snell's law. Instead, the light with polarization parallel to the OA experiences a higher refractive index n_e (*extraordinary ray*): a deflection occurs even when the incident light is orthogonal to the surface of the diffuser. As a result, the incident light is split into two rays having a small finite distance as shown in figure 1.

The optical diffuser from LaVision is composed of two birefringent plates having optical axes orthogonal to each other; these plates are separated by a glass plate between them. When using two diffusers, the incident ray is refracted to multiple spots on the camera sensor within a distance of 10 μm. Figure 2 shows the ray diagram for a coherent unpolarised ray of light passing through two diffusers. The optical axes of plates 2, 3 and 4 are at an angle of 90°, 45° and 135°, respectively, relative to the OA of plate 1. When the incident light ray passes through the first plate, it is split into two rays based on the light polarization, as discussed above. Since the second plate has OA orthogonal to that of the first plate, the second plate has the effect of causing the deflection of one of the two rays, without further splitting the rays. Hence, two light rays exit from the first diffuser. When these two rays interact with the plate 3, there is a 45° relative angle between the polarization of the incident ray and the OA of the plate. Hence, the incident light breaks down into two linear polarized components: a component parallel to the OA and another component perpendicular to the OA. Thus, the two incoming rays refracts into four rays as they come out from plate 3. Similarly, those rays get refracted into eight rays as they pass plate 4. Due to the lattice structure of the diffuser, the refracted rays are within the distance of 10 μm.

For any birefringent material, when the incident ray is at a polarization angle of 45° with respect to the OA, the intensity of the incident ray gets equally divided into two linearly polarised components having the same magnitude and oscillating at exactly the same phase as that of the incident ray (Murphy *et al* 2013). Hence, it is beneficial to keep the two diffusers at a relative angle of 45° as shown in figure 2.

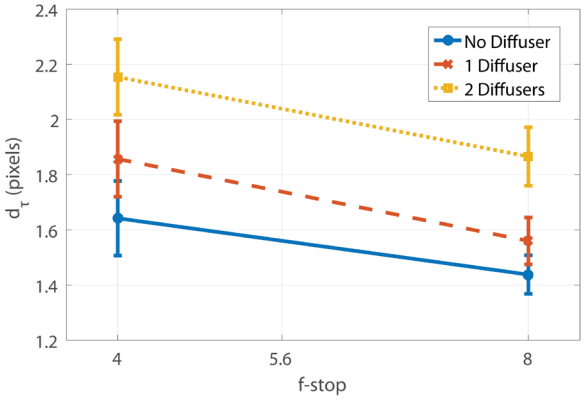

Figure 6. Image diameter estimation for 0/1/2 diffusers with standard uncertainty.

A dedicated experiment is conducted to evaluate the transmission efficiency of the optical diffusers. It is found that the diffusers have transmission efficiency of 99% and 96% for the green light (532 nm wavelength) and the white light, respectively. Hence, it is concluded that no significant reduction of the photon counts received by the camera sensor occurs when using the optical diffusers.

3. Experimental setup

To investigate the performances of the optical diffusers, experiments are conducted in the W-Tunnel of the Aerodynamics Laboratories of Delft University of Technology. The W-tunnel is an open jet wind tunnel with a square 0.4 × 0.4 m^2 test section. A maximum velocity of 35 m s^{-1} can be reached with a turbulence level of the order of 0.5%. The flow is seeded with Dantec SAFEX seeding generator, which produces water–glycol droplets of 1 μm median diameter. Images are recorded with a LaVision HighSpeedStar 6 camera (CMOS sensor, 1024 × 1024 px^2, 12 bits, pixel pitch of 20 μm, 5.4 kHz acquisitions frequency at full resolution), whose sensor size is cropped to 512 × 512 px^2. Image acquisition and processing are performed with the LaVision DaVis 8.3 software. In PIV processing, for reducing the background image, a time filter is used to subtract the minimum intensity from all images. A window deformation iterative multi-grid method (WIDIM, Scarano (2002)) is employed. For the measurement data, the initial interrogation window size is 64 × 64 px^2 with 50% overlap factor, whereas the final interrogation window size is

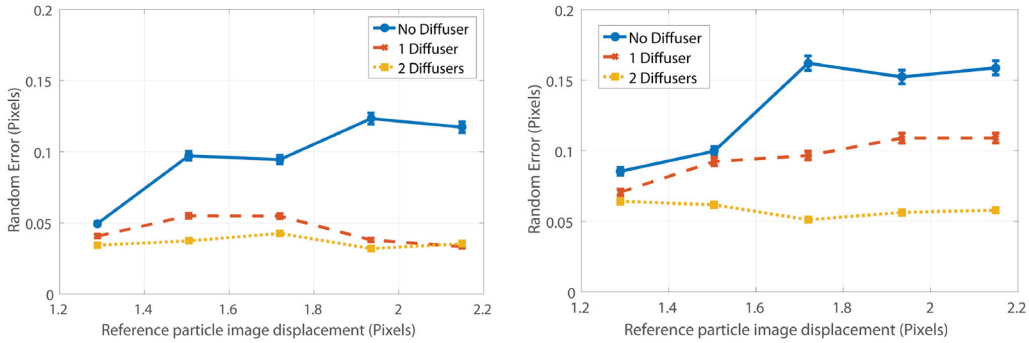

Figure 7. Random error as a function of the particle image displacement for 0, 1 and 2 optical diffusers with uncertainty bars calculated by standard deviation estimator (Lehmann and Casella 1998). Left: $f_{\#} = 4$; right: $f_{\#} = 8$.

16×16 px^2 with 75% overlap factor. For the reference data, the processing algorithm starts with window size of 256×256 px^2 with 75% overlap and ends with window size of 32×32 px^2 with 75% overlap. In all cases, a Gaussian weighting is applied to the interrogation window. For the image deformation, the interpolation of the pixel intensity at non-integer pixel locations is conducted by bilinear interpolation for the initial passes, and by B-spline interpolation on a kernel of 6×6 px^2 for the final passes. Symmetric image deformation is employed, meaning that both images of a pair are deformed by half of the calculated displacement.

Two flow cases are considered for the investigation of peak-locking error reduction by optical diffusers, namely uniform flow and wall-bounded turbulence. Details of the experimental setup of the measurements are reported below.

3.1. Uniform flow

The free-stream velocity, U_∞, is set to 15 m s^{-1}. A Quantronix Darwin-Duo laser (Nd:YLF diode pumped, 2×25 mJ pulse energy at 1000 Hz, wavelength of 527 nm) is installed below the test section. A mirror directs the laser beam upwards toward the test section. A combination of negative spherical lens and cylindrical positive lens is used to produce a laser sheet of 1 mm thickness in the measurement region. The camera is equipped with a Nikon objective of 105 mm focal length. The field of view (FOV) is 73 mm $\times$ 73 mm, yielding a magnification factor of 0.14. Measurements are repeated for two values of the f-number, namely $f_{\#} = 4$ and $f_{\#} = 8$, to investigate the effect of such parameter on the particle image diameter. At each *f*-number, measurements with 0, 1 and 2 optical diffusers are conducted. The inter-frame time separation (time delay between the recording of two frames for the double-frame camera images) is varied between 10 μs to 20 μs in steps of 2 μs to achieve a range of sub-pixel particle image displacements. A reference measurement is performed with optimal measurement conditions, namely $f_{\#} = 11$, slightly defocused images and inter-frame time separation of 340 μs; such parameters are selected to minimize the relative errors on the displacement due to peak-locking or additional sources (e.g. camera noise). For each test case, a set of 500 images is acquired. A sketch of the experimental setup is depicted in figure 3.

In a second experimental campaign, experiments are conducted at 15 m s^{-1} to investigate the performances of

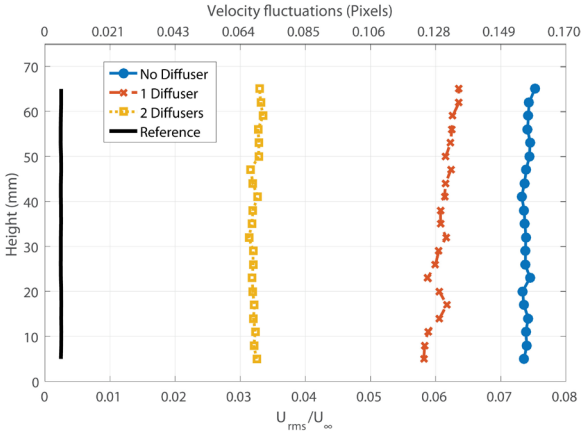

Figure 8. Fluctuations RMS velocity profile for uniform flow in an empty test-section at $f_{\#} = 4$.

the diffusers for different intensities of the light source. The camera mounts a Nikon objective of 60 mm focal length set to aperture of $f_{\#} = 4$. The camera sensor is cropped to 512×512 pixels and images a FOV is 95 mm $\times$ 95 mm, yielding a magnification factor of 0.11. The image acquisition is carried out in frame-straddling mode at a frequency of 200 Hz; one every five image pairs is stored to reduce the disk storage. For each run, an ensemble of 2000 image pairs is acquired to ensure statistical convergence of the results. The inter-frame time separation is set to 19 μs. The measurements are conducted with zero and two diffusers and with increasing the current for laser light intensity from 15 A to 25 A. The reference measurements are carried out with an inter-frame time separation of 190 μs and laser light intensity of 27 A.

3.2. Wall-bounded turbulence

The experiment is conducted at free-stream velocity, U_∞, of 20 m s^{-1}. The flow at the bottom wall of the wind tunnel test section is investigated. A zig-zag strip of 1 cm length and 1 mm height is installed 6.5 cm downstream of the test-section leading edge to ensure the turbulent regime of the boundary layer. The illumination is provided by a Mesa PIV laser (Nd:YAG diode pumped, 2×13 mJ pulse energy at 6000 Hz, wavelength of 532 nm). A Nikon objective of 105 mm focal length is mounted on the camera. The FOV (73 mm $\times$ 73 mm) is positioned on the centre line of the

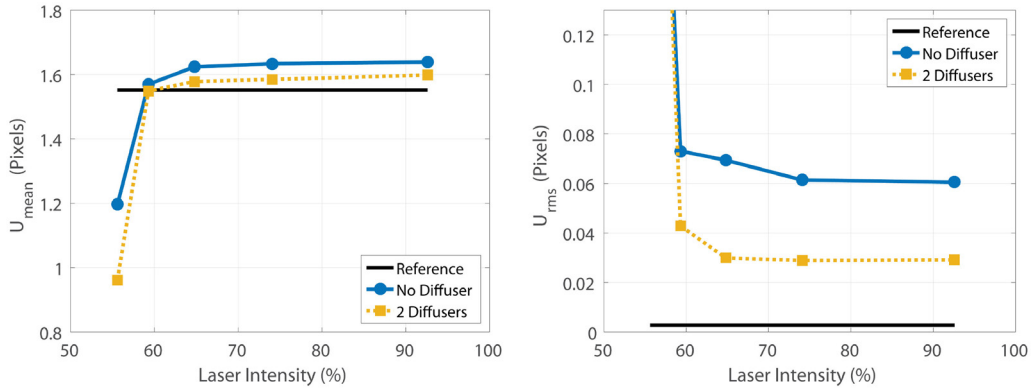

Figure 9. Mean velocity (left) and fluctuations RMS (right) for different intensity of the light source.

test-section floor at a distance of 48.5 cm from the test-section leading edge; the resulting magnification factor is 0.14. The experimental setup is shown in figure 4. The inter-frame time separation is set to 20 μs. The measurements are repeated for zero and two diffusers, and for f-numbers $f_\# = 4$, 5.6 and 8. In order to study the effect of image defocusing on the random and bias errors, measurements are also repeated by shifting the camera position along the direction of its OA, so to achieve different degrees of image defocusing. The camera position is varied from 0 mm (sharply focused images) to 25 mm (strongly defocused images) with steps of 5 mm. A low f-number ($f_\# = 4$) is chosen to obtain a small depth of field ($\delta z = 10$ mm).

The reference data are acquired with $f_\# = 5.6$ and slightly defocused images. The time separation is set to 80 μs. For each measurement test case, a set of 2000 images is acquired.

4. Data reduction

The reference measurements are conducted at an inter-frame time separation Δt_{aux}, which is larger than the time separation Δt_{meas} of the standard measurements; the bias and random errors on the particle image displacement of the latter need to be evaluated. The reference measurement yields an average particle image displacement (averaged in space and time for the uniform flow test case, only in time for wall-bounded turbulence test case) which is indicated with u_{aux}. For brevity, only the horizontal velocity component of the displacement is considered here. The particle image displacement from standard measurements is indicated with u_{meas}. Due to the optimal choice of the imaging parameters, the relative error on u_{aux} is negligible with respect to that on u_{meas}. In order to compare particle image displacements occurring at different time separation, the displacement u_{aux} (occurring in the time separation Δt_{aux}) is scaled to the time separation Δt_{meas}, obtaining the reference particle image displacement:

$$u_{\text{ref}} = u_{\text{aux}} \frac{\Delta t_{\text{meas}}}{\Delta t_{\text{aux}}}. \tag{1}$$

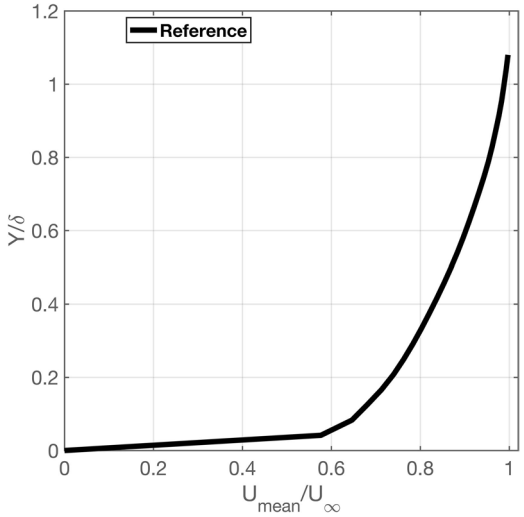

Figure 10. Time-average velocity profile for turbulent boundary layer test case. In the vertical axis, Y is normalized with respect to δ_{99}.

For the uniform flow test case, at each time separation Δt_{meas}, the measurement error on the particle image displacement is equal to

$$\varepsilon = u_{\text{meas}} - u_{\text{ref}}. \tag{2}$$

From the instantaneous measurement error, the mean bias and random errors are computed, indicated with ε_{b} and ε_{r}, respectively:

$$\varepsilon_{\text{b}} = \frac{\sum_{i=1}^{N} \varepsilon_i}{N} \tag{3}$$

$$\varepsilon_{\text{r}} = \sqrt{\frac{\sum_{i=1}^{N} (\varepsilon_i - \varepsilon_{\text{b}})^2}{N-1}}. \tag{4}$$

The parameter N in the summations of equations (3) and (4) is the total number of vectors in space and time.

Instead, for the wall-bounded turbulence test case only the bias error can be computed directly using equation (2), with u_{meas} the time-averaged velocity. Information on the random

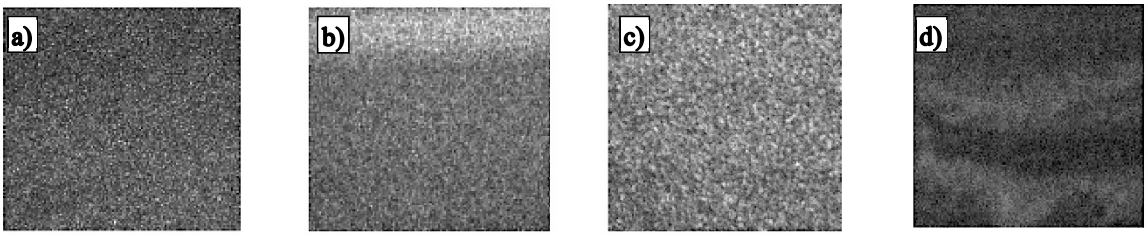

Figure 11. Raw PIV images showing the particle image diameter for (a) no diffuser; (b) two diffusers; (c) defocused images (and no diffuser), i.e. camera position @ 10 mm; (d) highly defocused images (and no diffuser), i.e. camera position @ 15 mm.

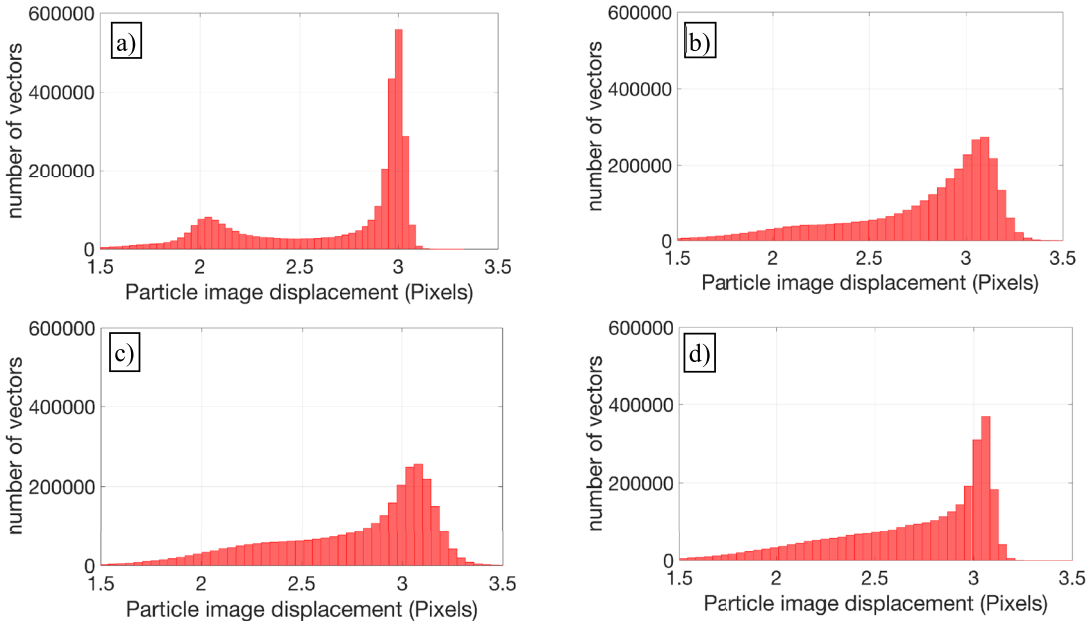

Figure 12. 1D displacement histogram for turbulent boundary layer profile; results for $f_{\#} = 4$. (a) No diffuser; (b) two diffusers; (c) defocused images (and no diffuser); (d) reference images ($f_{\#} = 5.6$, $\Delta t_{\text{aux}} = 4\ \Delta t_{\text{meas}}$).

errors is obtained by comparing the velocity fluctuations root-mean-square (RMS) profile.

5. Results

5.1. Uniform flow

The mean bias error as a function of the reference particle image displacement for $f_{\#} = 4$ and $f_{\#} = 8$ is shown in figure 5. When no optical diffuser is mounted on the imaging system, the typical sinusoidal behaviour of the mean bias error due to peak-locking is retrieved (Cholemari 2007). The errors are the highest for 0.25 and 0.75 pixels fractional displacements, where they reach 0.13 pixels and 0.25 pixels for $f_{\#} = 4$ and $f_{\#} = 8$, respectively. It may seem counterintuitive that the peak-locking error is larger for $f_{\#} = 8$, where the diffraction limited particle image diameter is larger (6.2 μm for $f_{\#} = 4$; 12.4 μm for $f_{\#} = 8$). However, one should keep in mind that the particle image diameter is not only due to diffraction and to the geometrical projection of the particle image (which in this case yields a negligible contribution of 0.2 μm), but it is also due to lens aberration. Since the lens aberration has a larger effect at lower $f_{\#}$, a larger particle image diameter is obtained at $f_{\#} = 4$ (1.65 pixels for $f_{\#} = 4$; 1.45 pixels for $f_{\#} = 8$, see figure 6), yielding reduced peak-locking errors. Here the particle image diameter is calculated as the e^{-2} width of the auto-correlation peak, according to Adrian and Westerweel (2011): $d_\tau = 2\sqrt{2}\sigma$, where σ is the standard deviation of the Gaussian fit applied to the auto-correlation peak. Notice that this method typically overestimates particle image diameters below 1 pixel, 1.19 pixels being the minimum diameter that can be measured. The uncertainty bars here show the standard deviation of the particle image diameter evaluated throughout the image.

When one optical diffuser is mounted on the imaging system, the mean particle image diameter increases to 1.85 pixels for $f_{\#} = 4$ and 1.55 pixels for $f_{\#} = 8$ (figure 6). The sinusoidal shape of the mean bias error as a function of the particle image displacement is maintained, but the amplitude of the peak-locking error is reduced by about a factor of 2 (figure 5) as a result of the increased particle image diameter. When two diffusers are employed, the particle image diameter is further increased to 2.15 pixels and 1.85 pixels for $f_{\#} = 4$ and 8, respectively. In this case, the mean bias error is reduced by a factor of 3 with respect to the zero-diffuser case and stays below 0.05 pixels in the entire range of particle image displacements. Furthermore, the sinusoidal trend of the error is not visible anymore.

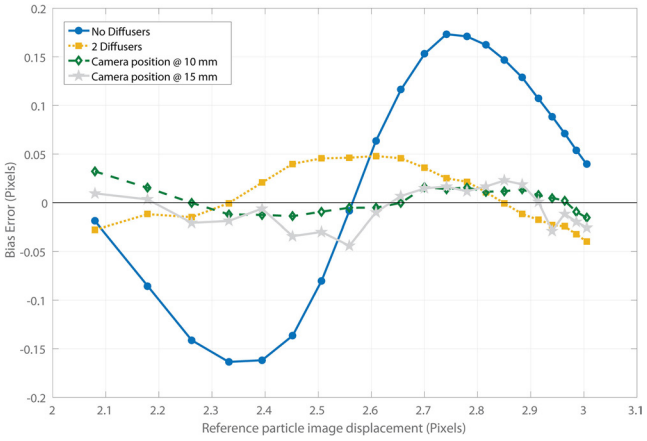

Figure 13. Bias error versus reference displacement for 0/2 diffusers and optical defocusing at $f_{\#} = 4$.

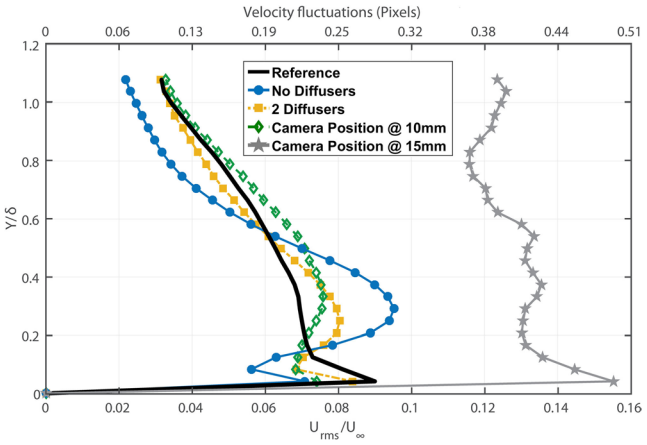

Figure 14. Fluctuations RMS velocity profiles for the turbulent boundary layer test case at $f_{\#} = 4$. In the vertical axis, Y is normalized with respect to δ_{99}.

The random error as a function of the reference particle image displacement is shown in figure 7 for $f_{\#} = 4$ and $f_{\#} = 8$. The uncertainty bars represent the standard uncertainty of the estimated random error, computed according to Lehmann and Casella (1998). In absence of the optical diffusers, the random error increases by about a factor of 2 in the considered range of particle image displacements. As for the mean bias error, also the random error is higher for the higher $f_{\#}$, which is attributed to the smaller particle image diameter. The use of optical diffusers reduces the random errors by a factor of 2 to 3. When two optical diffusers are employed, the highest reduction of random errors is achieved, with ε_r that stays constant in the entire range of particle image displacements.

The fluctuations RMS velocity profiles in the measurement domain are shown in figure 8. The reference velocity fluctuations are 0.25% or 0.005 pixels, which are due to the free-stream turbulence of the wind tunnel. The mean particle image displacement for the reference data is 35 pixels. When no diffuser is used, the velocity fluctuations are largely overestimated due to peak-locking, reaching values of 0.16 pixels. The estimated fluctuations drop significantly to 0.13 and 0.06 pixels when mounting one or two diffusers onto the imaging system, respectively, yielding a reduction of measurement errors by up to a factor of 3.

The mean velocity and fluctuations RMS are evaluated at different intensity of the light source to investigate the performance of the diffusers at low image signal-to-noise ratio (SNR) (figure 9). The laser current is varied between 15 A and 25 A, corresponding to 55% and 95% of the maximum intensity. The image SNR ranges between 1.2 and 10 (evaluated by visual inspection of particle and noise intensity). The results confirm that the two diffusers yield a reduction of both random and systematic errors by a factor of 2 to 3 also at low laser power (60% of total power, corresponding to image SNR of 2). Only at very low image SNR, errors of both no-diffuser and 2-diffuser configurations are of the order of 0.5 pixels or above due to the presence of outliers in the measured vector field.

5.2. Wall-bounded turbulence

The boundary layer properties are characterized from the reference data. The boundary layer thickness is $\delta_{90} = 14.8\,\text{mm}$, whereas displacement thickness and momentum thickness are $\delta^* = 4.3\,\text{mm}$ and $\theta = 2.9\,\text{mm}$, respectively. The resulting shape factor is $H = 1.5$, which confirms the turbulent regime of the boundary layer (White and Corfield 2006). Figure 10 shows the time-average velocity profile of the reference data for the turbulent boundary layer.

The particle image diameter is estimated from e^{-2} width of the auto-correlation peak as 1.5 pixels, 2.1 pixels, 2.2 pixels and 3.5 pixels for no diffuser, two diffusers, slightly defocused camera images and largely defocused camera images respectively. Figure 11 shows the raw PIV images for above mentioned particle image diameter. The effect of peak-locking on the 1D displacement histogram is shown in figure 12. The reference histogram (figure 12(d)) does not exhibit any peak at integer pixel displacement, meaning that the reference data contains negligible peak-locking errors. Conversely, high peaks at integral values of the pixel displacement are visible for the no diffuser case (figure 12(a)), clearly indicating severe peak-locking in the images. For the two-diffuser case (figure 12(b)), the peaks height is strongly decreased and the histogram flattens due to the favourable effect of the two diffuser. Similar results are also obtained by the best optical defocussed position without any diffuser as shown in figure 12(c).

The mean bias error as a function of reference particle image displacement for no diffusers, two diffusers and optically defocused camera position for $f_{\#} = 4$ is shown in figure 13. For no diffusers, the sinusoidal nature of the bias error is evident, where the mean bias error is minimum close to integer displacement values and maximum at 2.35 pixels and 2.75 pixels displacements. The maximum mean bias error is equal to 0.17 pixels. For two diffusers and best defocusing (focal plane shifted by 10 mm with respect to the measurement plane), the sinusoidal trend of the bias error is not visible anymore, and the maximum error is reduced to below 0.05 pixels. The performance of the two diffusers is comparable with that of optimal image defocusing practice. Also when

the images are largely defocused (focal plane shifted by 15 mm with respect to the measurement plane) the mean bias error stays below 0.05 pixels in the entire range of sub-pixel displacements.

The fluctuations RMS velocity profiles for reference data, no diffusers, two diffusers, slightly defocused camera images and largely defocused camera images are shown in figure 14. The velocity fluctuations are the maximum at about $Y/\delta = 0.05$, reaching a value of 9% U_∞. For the no-diffuser case, the velocity fluctuations are largely misjudged, with differences up to 0.08 pixels with respect to the reference fluctuations: they are overestimated in $0.15 < Y/\delta < 0.55$, and underestimated in the rest of the profile. This behaviour is clearly attributed to peak-locking, which has the effect of underestimating fluctuations with sub-pixel displacement between 0 and 0.5 pixels, and overestimating fluctuations with sub-pixel displacement between 0.5 and 1 pixels. For the two-diffuser case and the optimal defocusing case (camera position @ 10 mm), the discrepancy between measured and reference fluctuations reduces to below 0.03 pixels, thus yielding a reduction of measurement errors by almost a factor of 3 with respect to the no-diffuser case. When the camera images are largely defocused (15 mm separation between focal plane and measurement plane), the flow fluctuations are largely overestimated (by up to 0.2 pixels) due to the increased random errors in the displacement measurements. This result evidences that care must be taken when defocusing the camera images, so to ensure that peak-locking errors are reduced without leading to increased random errors due to blurred particle images.

6. Conclusion

In this paper, the reduction of peak-locking errors by means of optical diffusers mounted between the camera sensor and the camera lens has been investigated. Experiments have been conducted on uniform flow and turbulent flow to quantify the peak-locking errors reduction. In all cases, a reference velocity measurement was available from acquisition conducted with optimal imaging conditions and with larger time separation between laser pulses. The peak-locking errors with no, one and two diffusers have been quantified. Additionally, comparisons have been conducted with image defocusing, which is considered the standard practice for reduction of peak-locking errors.

It has been shown that the use of optical diffusers yields an increased particle image diameter; the increase is larger when two diffusers are applied. Comparison with the reference measurements showed a reduction of both systematic and random error components by a factor of 3 with respect to standard in-focus imaging, where no diffuser is mounted on the camera. The performances of the diffusers are not degraded even at imaging SNR as low as 2. The error reduction obtained with two optical diffusers is comparable with that achieved by optimal image defocusing. However, it is shown that excessive image defocusing yields increased random errors, thus reducing the overall accuracy of the measurements. The use of the diffusers allows more repeatable error reductions, because always the same increase of particle image diameter is achieved and no optimal tuning is required, contrary to image defocusing. Furthermore, their use can be extended to 3D PIV measurements, where image defocusing is clearly not applicable.

Acknowledgments

Bernd Wieneke from LaVision GmbH is kindly acknowledged for providing the optical diffusers and for the numerous useful discussions on the working principle of the diffusers.

ORCID iDs

Ankur Kislaya https://orcid.org/0000-0002-8011-8505
Andrea Sciacchitano https://orcid.org/0000-0003-4627-3787

References

Adrian R J and Westerweel J 2011 *Particle Image Velocimetry* (Cambridge: Cambridge University Press)
Angele K P and Muhammad-Klingmann B 2005 A simple model for the effect of peak-locking on the accuracy of boundary layer turbulence statistics in digital PIV *Exp. Fluids* **35** 341–7
Astarita T and Cardone G 2005 Analysis of interpolation schemes for image deformation methods in PIV *Exp. Fluids* **38** 233–43
Born M and Wolf E 1999 *Principles of Optics* 7th edn (Oxford: Pergamon)
Chen J and Katz J 2005 Elimination of peak-locking error in PIV analysis using the correlation mapping method *Meas. Sci. Technol.* **16** 1605–18
Cholemari M R 2007 Modelling and correction of peak-locking in digital PIV *Exp. Fluids* **42** 913–22
Christensen K T 2004 The influence of peak-locking errors on turbulence statistics computed from PIV ensembles *Exp. Fluids* **36** 484–97
Fore L B 2010 Reduction of peak-locking errors produced by Gaussian sub-pixel interpolation in cross-correlation digital particle image velocimetry *Meas. Sci. and Technol.* **21** 035402
Gui L and Wereley S T 2002 A correlation-based continuous window-shift technique to reduce the peak-locking effect in digital PIV image evaluation *Exp. Fluids* **32** 506–17
Hearst R J and Ganpathisubramani B 2015 Quantification and adjustment of pixel-locking in particle image velocimetry *Exp. Fluids* **56** 1–5
Lehmann E L and Casella G 1998 *Theory of Point Estimation* (New York: Springer)
Michaelis D, Neal D R and Wieneke B 2016 Peak-locking reduction for particle image velocimetery *Meas. Sci. Technol.* **27** 104005
Murphy D B, Spring K R, Fellers T J and Davidson M W 2013 *Principles of Birefringence* (Nikon Instruments Inc.) (www.microscopyu.com/techniques/polarized-light/principles-of-birefringence)
Nobach H, Damaschke N and Tropea C 2005 High-precision sub-pixel interpolation in particle image velocimetry image processing *Exp. Fluids* **39** 299–304
Nogueira J, Lecuona A and Rodríguez P A 2001 Identification of a new source of peak locking, analysis and its removal in conventional and super-resolution PIV techniques *Exp. Fluids* **30** 309–16

Nogueira J, Lecuona A, Nauri S, Legrand M and Rodríguez P A 2009 Multiple Δt strategy for particle image velocimetry (PIV) error correction, applied to a hot propulsive jet *Meas. Sci. Technol.* **20** 074001

Nogueira J, Lecuona A, Nauri S, Legrand M and Rodríguez P A 2011 Quantitative evaluation of PIV peak locking through a multiple Δt strategy: relevance of the rms component *Exp. Fluids* **51** 785–93

Overmars E F J, Warncke N G W, Poelma C and Westerweel J 2010 Bias errors in PIV: the pixel locking effect revisited *15th Int. Symp. on Applications of Laser Techniques to Fluid Mechanics (Lisbon, Portugal)*

Raffel M, Willert C, Wereley S and Kompenhans J 2007 *Particle Image Velocimetry: a Practical Guide* (New York: Springer)

Roesgen T 2003 Optimal subpixel interpolation in particle image velocimetry *Exp. Fluids* **35** 252–6

Roth G I and Katz J 2001 Five techniques for increasing the speed and accuracy of PIV interrogation *Meas. Sci. Technol.* **12** 238–45

Scarano F 2002 Iterative image deformation methods in PIV *Meas. Sci. Technol.* **13** R1–19

Scarano F and Reithmuller M L 1999 Iterative multigrid approach in PIV image processing with discrete window offset *Exp. Fluids* **26** 513–23

Westerweel J 1993 Analysis of PIV interrogation with low-pixel resolution *Proc. SPIE* **2005** 624–35

Westerweel J 1997 Fundamentals of digital particle image velocimetry *Meas. Sci. Technol.* **8** 1379–92

White F M and Corfield I 2006 *Viscous Fluid Flow* vol 3 (New York: McGraw-Hill)